Eur. Phys. J. B (2022)95:96
https://doi.org/10.1140/epjb/s10051-022-00354-5

THE EUROPEAN
PHYSICAL JOURNAL B

Regular Article - Statistical and Nonlinear Physics

Emergence of multi-stability and limit cycles in ferromagnetic spin-crossover solids under an oscillating magnetic-field: dynamic mean-field study

T. D. Oke[1,2,a], S. B. Ogou[1,2], F. Hontinfinde[1], and K. Boukheddaden[2,b]

[1] Département de Physique: Faculté de Sciences et Techniques (FAST) et Institut de Mathématiques et de Sciences Physiques (IMSP), Université d'Abomey-Calavi (UAC), Porto-Novo 01 BP 613, Benin
[2] Université Paris-Saclay, UVSQ, CNRS, GEMAC UMR 8635, 45 Avenue des Etats Unis, Versailles Cédex, France

Received 3 March 2022 / Accepted 13 May 2022

Abstract. Two dimension (2D) Blume–Emery–Griffiths (BEG) spin-1 model is used to investigate spin-crossover (SCO) and Prussian Blue Analogs (PBAs) solids. The model considered here allows the system to switch between two fundamental spin states named high-spin (HS) and low-spin (LS) states subsequent to the strength of magnetic and elastic interactions which acting on lattice nearest neighbors sites. These interactions are assumed as temperature-dependent due to the system volume changes accompanying with the spin transition phenomenon. In addition, SCO molecules are subject to a variable frequency of magnetic-field lifting the degeneracy in the HS state. A stochastic cooperative dynamics of this BEG-like Hamiltonian, describing the nonequilibrium properties of ferromagnetic SCO solids, is derived from the Glauber approach, with appropriate Arrhenius microscopic transition rates. At the vicinity of the thermal hysteresis loop of the free system (obtained with zero-magnetic field), investigations with variable oscillation frequency of the magnetic-field, h, demonstrated significant changes on the isothermal relaxation curves of the magnetization, m, and the high-spin fraction, n_{HS}, which fall down on dynamical equilibrium characterized by limiting cycles in the spaces m-h and n_{HS}-h. In addition, the clear evidence of dephasing between the responses of the two order parameters (m and n_{HS}) and the particular "butterfly" shape of the limiting cycles of the HS fraction, enforces the idea that the non-linear effects, propagating through the interaction parameters, are operating in this system. These behaviors demonstrate that radio-frequency magnetic field can be used in these SCO systems to achieve a reversible switch and control of both magnetization and HS fraction, even if the latter is partial. These results are in direct relation with the intrinsic static multi-stability of the system under static magnetic-field, which is enhanced/revealed by applying an oscillating magnetic-field.

1 Introduction

Recently, the family of transition-metal complexes have continued to attract more attentions of physicists and chemists scientists because of their rich physical properties [1–5] which open serious potentialities of their utilization in advanced technologies as miniaturized devices with fast response in the field of the treatment and reversible storage of information. Commonly named spin crossover (SCO) materials, they have $4 \sim 7d$-electrons in outer metallic configurations and usually exhibit high-spin (HS) and low-spin (LS) configurations due to competition between the Pauli exclusion principle and the crystal-field energy. Such materials can undergo phase transitions under various stimuli such as, emitting light, variations of temperature, pressure, generating magnetic and electric fields, etc. [6–12]. In specific conditions, thermally-induced spin transitions in SCO materials lead to both electronic and structural changes, often observed as a color and global magnetic changes [1,13,14]. Then, spin-transition occurs according to the strength of interactions between SCO units: for weak interactions, the HS fraction undergoes a smooth and continuous change when the temperature is increased whereas, first-order transitions appear [15–17] with large thermal hysteresis when these interactions become strong enough. The common example cited in litera-

---

We dedicate the present work to the memory of our colleague Dr. Yogendra Singh who passed away prematurely these days.

Supplementary Information The online version contains supplementary material available at https://doi.org/10.1140/epjb/s10051-022-00354-5.

[a] e-mail: toussaint.oke@imsp-uac.org (corresponding author)

[b] e-mail: kamel.boukheddaden@uvsq.fr (corresponding author)

ture that exhibits such transition near room temperature, is that of the $[\mathrm{F}_e(\mathrm{NH_2trz})_3)](\mathrm{NO}_3)_2$, ($\mathrm{NH_2trz}$ = 4-amino-1, 2, 4-triazole) [18]. Of course, the SCO transition results from the microscopic changing of unit-cell volume and bond length that are considerably larger in the HS state. In addition, beside the larger electronic degeneracy which emerges, a larger phonon density of the HS is also obtained [15,16,19]. At the atomic scale, SCO complexes based on $\mathrm{F}_e(II)$ metal center, exhibit two spin states, a paramagnetic high-spin (HS, $e_g^2t_{2g}^4, \sigma = 2$) state, stable at high temperatures and a diamagnetic low-spin (LS, $e_g^0t_{2g}^6, \sigma = 0$) state, stable at low temperatures. Then, the SCO phenomenon appears as resulting from the redistribution of the electrons between the bonding t_{2g} and the antibonding e_g orbitals. Indeed, elastic interactions [20–39] are recognized as a basic ingredient to govern SCO transitions which involve both electronic transformation (spin and orbital) and structural modifications [35,40–44] as demonstrated experimentally.

Moreover, SCO phenomena have been described within Ising-like models where the cooperativity between Ising spins is included through the exchange interactions [45,46] and accompanied somehow with magnetic-field to pointing out their physical properties. Being say, the first proposed a theoretical model by Sasaki and Kambara [47] with effect of a magnetic field based on Jahn-Teller interaction is used for prediction in large fields $(20 - 100$ T). Successively, with static and pulsed magnetic field in the range of $30 - 100$ T, meaningful results have been obtained with optical reflectivity detection technique on some molecular complexes as $\mathrm{F}_e(\mathrm{phen})_2(\mathrm{NCS})_2$, [phen=ortho-phenantroline] [48,49]; $\mathrm{Co(H_2(fsa)en)py_2}$, where $[\mathrm{H_2(fsa)en}]$ = N,N'-ethylene bis(3-carboxysalicylaldimine), py=pyridine] [49,50] and in diluted complexes $[\mathrm{Fe}_x\mathrm{Ni}_{1-x}(\mathrm{btr})_2(\mathrm{NCS})_2].\mathrm{H_2O}$, btr = $4', 4'$-Bis(1, 2, 4-triazole) [49] or with pulsed magnetic field and pressure[51]. For studying the microscopic local structure of $[\mathrm{Mn}^{III}(\mathrm{taa})]$, [$H_3$taa = tris(1−(2-azolyl)−2−azabuten-4-yl)amine] [52] in pulsed high magnetic fields up to 37 T, X-ray absorption near-edge structure (XANES) spectroscopy is a powerful tool for this type matter investigations. However, experimental results are achieved in Ref. [53] at low temperature during the investigation of the M_n^{III}[(pyrol)$_3$tren] in the presence of low magnetic-field of the order of 23 T. The (pyrol)$_3$tren is the trianomic Schiff base obtained from the condensation of pyrolle-2-carboxaldehyde with $2, 2', 2''$-tris(ethylamino)amine. Recently, Ogou et al. [54] have used kinetic spin-1 Blume–Emery–Griffiths (BEG) hamiltonian in the presence of a time-dependence magnetic-field to reproduce significant results on SCO materials. In the presence of time-dependent sinusoidal field, the model is described in dynamic mean-field theory (DMFT) approach where the obtained results are compared to those obtained by kinetic Monte-Carlo (KMC) simulations. Thermal properties and relaxation of metastable states are studied with the effects of the magnetic-field energy on the spin transitions. Also, under a static magnetic-field energy investigations, the generated results of the model exhibit isothermal sigmoidal relaxation and a hysteresis phenomenon of the HS fraction, as well as multistep behavior of the magnetization [55].

In the present investigations, the SCO is described using the BEG hamiltonian model as in Ref. [54] under time-dependent magnetic-field energy. SCO units interacted magnetically (in HS states) with temperature-dependent interactions [54–58] expressed as atom-phonon coupling. Then, the quadrupolar interaction is assumed to depend linearly on the absolute temperature as $K = \alpha K_B T$ accounting for spin-phonon interactions. The exchange magnetic interaction J is controlled by the parameter γ where $\gamma = J/K$. Due to the lattice distortion originated from the spin-transition that governed by elastic interactions, the lattice structure changes and affects the bond length between the metal center (usually in F_e^{II} cases) and the ligand atoms. The effective "ligand-field" energy D depends on the absolute temperature and contains the combined effects of the ligand-field strength Δ and that of the degeneracy ratio g between LS and HS states which results in an entropic term, stabilizing the HS state at high temperature. Here, the model is solved in the framework of DMFT approach. The nonequilibrium properties of the system are described from the obtained motion equations of the order parameters $m = \langle\sigma\rangle$ (magnetization) and $n_{HS} = \langle\sigma^2\rangle$ (HS fraction). These equations are derived from the Glauber dynamics with suitable Arrhenius transition rates. With series of magnetic-field frequencies controlled by the parameter λ in the oscillated component magnetic-field energy, n_{HS} and m show isothermal non-linear and limiting cycles as function of the field that are in some conditions, like magnetic hysteresis loop in the equilibrium states.

The paper is organized as follows. Section 2 contains the presentation of the BEG model, adapted for SCO systems and the description of the calculation method. In Sect. 3, we present and discuss the obtained results and in Sect. 4, we conclude.

2 Hamiltonian model description

SCO materials are described with the adapted spin-1 BEG model as subject to an oscillating magnetic-field energy and taking into account for magnetic and elastic interactions between SCO units. This Hamiltonian writes as follows [54]:

$$H = -J \sum_{<i,j>} \sigma_i \sigma_j - K \sum_{<i,j>} \sigma_i^2 \sigma_j^2 + D \sum_i \sigma_i^2 - h(t) \sum_i \sigma_i, \tag{1}$$

where $\sigma_i = \pm 1, 0$ are the fictitious spin values located at site i of the square lattice. The spins values $\sigma_i = \pm 1$ describe the magnetic HS spin state, whereas $\sigma_i = 0$ is associated with the diamagnetic LS state. According to the $2D$ character of the system, and to the square symmetry of the lattice, nearest-neighbor (nn) interactions are considered [54,55]. As in the previous works [31,32,45,46,54–58], the magnetic interactions between the magnetic states, $\sigma_i = \pm 1$, are taken into account through the exchange term, J. K (with $J/K = \gamma$) represents the quadrupolar interactions (between nn SCO sites) are introduced to be linearly dependent on temperature through, $K = \alpha k_B T$ where α is parameter constant. This last term takes into account for the phonon contribution which also originates from the intra-molecular vibrations, lattice distortion and/or acoustic phonons, which provide the elastic long-range interactions between the SCO units. $D = \Delta - k_B T \ln(g)$ [31,32,54–58] is the effective ligand-field strength and h [54,55] is the energy associated with the application of an external magnetic-field. In the following, a radio frequency magnetic-field

$$h(t) = h_0 \cos(\lambda \omega_0 t), \tag{2}$$

where ω_0 is the pulsation, proportional to the oscillation frequency which is controlled by the parameter $\lambda \in [0-1]$ in the temporal oscillations schemes.

2.1 Dynamic Mean-Field Theory (DMFT) formulation

Accounting for the long-range spin interactions throughout the lattice configurations, each spin located at site, i, feels the following one-site Hamiltonian, H_i in mean-field theory:

$$H_i(\sigma) = -z\mathrm{Jm}\sigma_i - z\mathrm{Kn}_{HS}\sigma_i^2 + D\sigma_i^2 - h(t)\sigma_i, \tag{3}$$

where, the order parameters, $m =< \sigma_i >$ and $n_{HS} =< \sigma_i^2 >$, are considered as invariant by translation over the lattice.

The energy gain of the evolving system is accounted-for as mean-field free energy per site given by Refs. [54,55]:

$$F(m, n_{HS}, T) = U - TS, \tag{4}$$

where U and S are the internal energy and entropy per site of the system, respectively, given by:

$$U = -\frac{z}{2}Jm^2 - \frac{z}{2}Kn_{HS}^2 + Dn_{HS} - h(t)m; \tag{5}$$

$$S = k_B \beta < H_i(\sigma_i) > + k_B \ln \sum_{\sigma_i} e^{-\beta H_i(\sigma)}, \tag{6}$$

where $\beta = \frac{1}{k_B T}$ (T is the absolute temperature, z is the lattice coordinence ($z = 4$ for the considered 2D lattice) and k_B is the Boltzmann constant) and $< H_i(\sigma_i) >= -zJm^2 - zKn_{HS}^2 + Dn_{HS} - h(t)m$ is the average value of $H_i(\sigma)$. After some calculations, the free energy per site is given by:

$$F(m, n_{HS}, T) = \frac{z}{2}Jm^2 + \frac{z}{2}Kn_{HS}^2 - k_B T \ln \left[1 + 2e^{\beta(zKn_{HS} - D)} \cosh \beta(zJm + h(t))\right]. \tag{7}$$

2.2 Dynamic choice and equations of motion

As in Refs. [54,55], the dynamical properties of the Hamiltonian (1) are investigated in the frame of microscopic master equation which governs the time evolution of the probability $P(\{\sigma_i\}, t)$ to occupy the spin configuration $\{\sigma\}$ at time t [44,54,55,57–60]. The expression of the flux of probability, $\frac{\partial P(\{\sigma\}, t)}{\partial t}$ accounts for stochastic transition from the configuration $\{\sigma\}_i \rightleftarrows \{\sigma'\}_i$ with transition rates W. The suitable Glauber-type stochastic dynamic is applied to obtain the mean-field dynamic equations of motion following the master equation:

$$\frac{\partial P(\{\sigma\}, t)}{\partial t} = -\sum_{i=1}^{N} W_i(\sigma_i \to \sigma_i^{'}) P(\{\sigma\}_i, \sigma_i, t) + \sum_{i=1}^{N} W_i(\sigma_i^{'} \to \sigma_i) P(\{\sigma\}_i, \sigma_i^{'}, t), \tag{8}$$

where $W_i(\sigma_i \to \sigma_i')$ is the transition rate of the ith spin changing from the value σ_i to σ_i' with respects to the specific Arrhenius spin-flip:

$$W_i(\sigma_i \to \sigma_i') = \frac{1}{3\tau} \frac{e^{-\beta H_i(\sigma_i')}}{\sum_{\sigma_i} e^{-\beta H_i(\sigma_i)}}. \tag{9}$$

Here, τ stands for the Arrhenius time scale and $\frac{1}{\tau}$ denotes the effective intramolecular frequency associated with the "spontaneous spin reversals"[54,55,57–60]:

$$\frac{1}{\tau} = \frac{1}{\tau_0} e^{-\beta E_0^a} \tag{10}$$

where $1/\tau_0$ the "intrinsic" frequency spin-flip process between HS and LS states, taken as constant and E_0^a is the intramolecular vibronic energy barrier, which originates from the volume change of the molecule subsequent to the spin state change between the LS and the HS states [61].

In equilibrium thermodynamics, the probabilities satisfy the detailed balance condition:

$$\frac{W(\sigma_i \to \sigma_i')}{W(\sigma_i' \to \sigma_i)} = \frac{P_{eq}(\{\sigma\}_i, \sigma_i', t)}{P_{eq}(\{\sigma\}_i, \sigma_i, t)}, \tag{11}$$

where $P_{eq}(\{\sigma\}_i, \sigma_i')$ is the Boltzmann probability to occupy the lattice site i by σ_i'. Thus, these transition rates, W, must fulfill the detailed balance condition and are expressed by:

$$W_i(\sigma_i \to \sigma_i') = W_i(\sigma_i') = \frac{1}{3\tau} \frac{e^{-\beta H_i(\sigma_i')}}{1 + 2e^{\beta(zKn_{HS} - D)} \cosh \beta(zJm + h(t))} \tag{12}$$

.

The mean value of the two relevant spin operators, σ_k and σ_k^2 respectively associated to the magnetization $m = \langle \sigma \rangle$ and HS fraction, $n_{HS} = \langle \sigma^2 \rangle$, are calculated as follows:

$$m = \sum_{\{\sigma\}} \sigma_k P(\{\sigma_k\}, t) \quad \text{and} \quad n_{HS} = \sum_{\{\sigma\}} \sigma_k^2 P(\{\sigma_k\}, t), \tag{13}$$

and $\sum_{\sigma'_k \neq \sigma_k} W_k(\sigma'_k) = \frac{1}{3\tau}$. By combining Eqs. (8), (12) and (13), one gets, after some calculations, the time evolution of the magnetization m and the HS fraction n_{HS} which are expressed as analytical non-linear coupled differential equations:

$$\begin{cases} \frac{dm}{dt} = \frac{e^{-\beta E_0^a}}{3\tau_0} \left(-m + \frac{2\sinh\beta(z\mathrm{Jm}+h(t))}{e^{-\beta(z\mathrm{Kn}_{HS}-D)}+2\cosh\beta(z\mathrm{Jm}+h(t))} \right) \\ \frac{dn_{HS}}{dt} = \frac{e^{-\beta E_0^a}}{3\tau_0} \left(-n_{HS} + \frac{2\cosh\beta(z\mathrm{Jm}+h(t))}{e^{-\beta(z\mathrm{Kn}_{HS}-D)}+2\cosh\beta(z\mathrm{Jm}+h(t))} \right) \end{cases}. \tag{14}$$

Equation (14) are numerically solved by using fourth order Adams-Moulton predictor-corrector methods [62–65].

Here, the magnetic-field energy depends on time as $h(t) = h_0 \cos(\lambda\omega_0 t)$, where, by setting $\xi = \omega_0 t$, ω_0 becomes a simple parameter and we considered ξ as the control parameter in time. The dynamical properties of the system will be analyzed below as a function of the absolute temperature T and magnetic-field energy, h with variables frequencies controlled by the parameter λ.

3 Results and discussions

In this section, thermodynamic quantities are presented for a ferromagnetic SCO system under magnetic-field energy from the point of view of their non-equilibrium properties. For simplicity, the individual spin-flip frequency is set to the value $\frac{1}{3\tau_0} = 1\ s^{-1}$ and the activation energy to $E_0^a = 0\ K$. Qualitatively, similar results can be reproduced with these parameters different to these values. Then, the ligand-field energy is set to the value of $\Delta = 400\ K$ and the degeneracy ratio value between LS and HS is represented by $g = 100$. First, we analyze the physical properties of the system at thermal equilibrium in zero magnetic-field energy.

3.1 Equilibrium properties

As in Fig. 1 of Ref. [55], the thermal equilibrium properties of the system are derived from the analysis of the stationary states ($\frac{\partial m}{\partial t} = 0$ and $\frac{\partial n_{HS}}{\partial t} = 0$) where the system is time independent. The couple of self-consistent equations (14) of state of the system are given by change now to Eq. (15), describing the thermal dependence of the HS fraction (n_{HS}) and magnetization (m) in the framework of the Mean-Field Theory (MFT) in the absence of external magnetic field, although the equation of states (Eqs. 15) are given here in the general case.

$$\begin{cases} m = n_{HS} \tanh\left(\beta\left(zJm + h\right)\right) \\ n_{HS} = \frac{2\cosh(\beta(zJm+h))}{e^{-\beta(zKn_{HS}-D)}+2\cosh(\beta(zJm+h))} \end{cases}. \tag{15}$$

These equations (Eq. 15) are solved using the Newton–Raphson method, by setting $h = 0$, in the interval $10 - 70$ K with temperature step $\Delta T = 1.\ K$ and for selected values of model parameters. For $\alpha = 3$ and $\gamma = 0$ ($\alpha = K/k_B T$, $\gamma = J/K$) i.e. without any magnetic coupling, Fig. 1a, b display the thermal behaviors of the magnetization m and the HS fraction, n_{HS}. The spin transition that appeared on n_{HS} is of first-order where the obtained thermal hysteresis loop is in the range of $28 - 47$ K. In this domain, three solutions of spin states are obtained for n_{HS}: stable, metastable and unstable and beyond that, stable states are got. For low temperatures, the magnetic system stays diamagnetic ($\langle\sigma\rangle = 0$ and $\langle\sigma^2\rangle = 0$) in the LS state and becomes paramagnetic ($\langle\sigma\rangle = 0$ and $\langle\sigma^2\rangle = 1$), at high temperatures, in the HS state, whereas for enhanced magnetic coupling as in the case of Fig. 1c, d ($\gamma = 2$, $\alpha = 1$) first-order spin transition occurs with hysteresis loop in the temperatures range $30 - 52$ K with five and three solutions of spin states, respectively of m and n_{HS} which are in nature: stable, metastable and unstable states again. The magnetization $m = 0$ is still a trivial solution at all temperatures (see Eq. (15)) but new solutions appear in the thermal dependence of n_{HS} and nonzero solutions exist for $m(T)$, which shows now a thermally-induced magnetic first-order transition.

Moreover, we look for adding some of isothermal stationary properties of the system studied for helping the reader to understand the multi-spin states transition that occur belong applying the static magnetic-field energy. Indeed, the spin-transition occurs in the vicinity and inside of the thermal hysteresis loops (see Fig. 1) in the absence/presence of the magnetic interactions (see Figs.2 and 3 of Ref. [55]). For varying the field between +200 and −200 K and at fixed temperature ($T = 30, 35$ and 50 K), Fig. 2 shows different spin states created by static magnetic-field in the case of $\gamma = 0$, whereas magnetic properties are depicted in Fig. 3 with $\gamma \neq 0$ for $T = 30, 35$ and 40 K. We denote that, the magnetic-field energy is responsible of the multi-spin transition accompanied with magnetic hysteresis-like where appear different states in stable, metastable and unstable domains according to the temperature values.

3.2 Isothermal relaxation of the system under oscillating field with $\lambda = 1$

Following the thermal hysteresis of Fig. 1, the effects of external magnetic-field constraint on SCO compounds

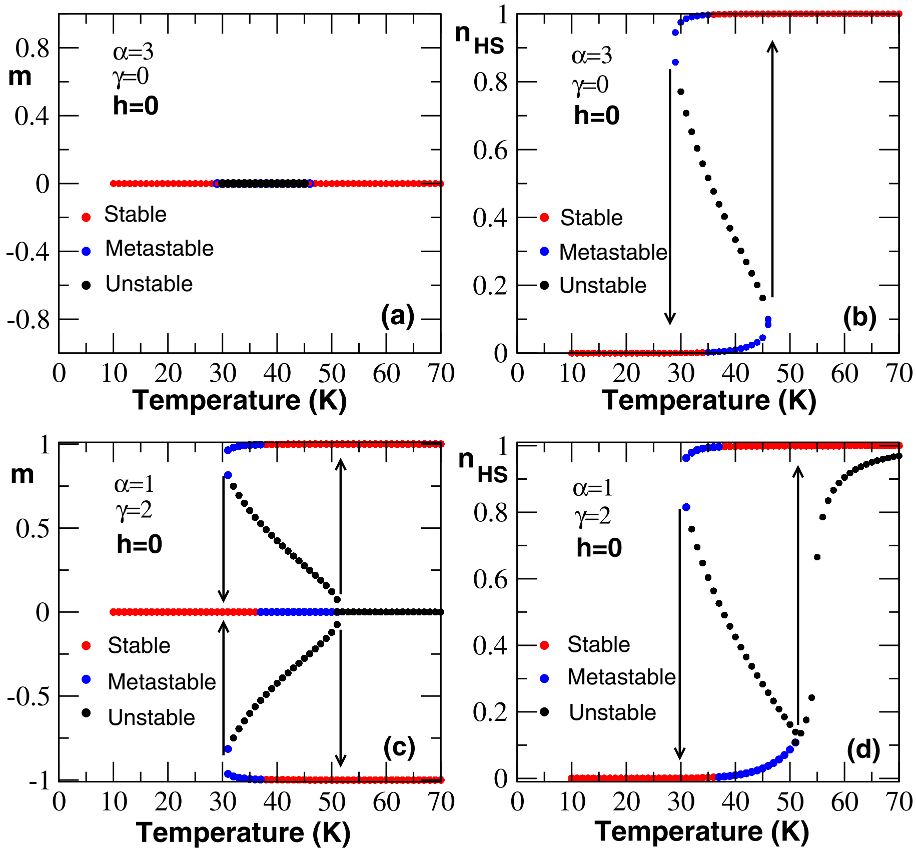

Fig. 1 Thermal behavior of magnetization m and n_{HS} fraction in the absence of magnetic-field energy ($h = 0$). First-order spin-transition is obtained with sigmoidal shapes in their behaviors for selected values of α and γ. Panels **a** and **b** are obtained for $\alpha = 3$ and $\gamma = 0$. There, $m = 0$ whereas HS fraction, n_{HS} raises from LS to HS state through intermediate states. In Panels **c** and **d**, different states are depicted through m and n_{HS} behaviors for $\alpha = 1$ and $\gamma = 2$. Different color codes, red, blue and black are used here to identify stable, metastable and unstable states, respectively

have been studied from the theoretical point of view in Refs. [54,55]. Thus, Fig. 4 summarizes, at fixed temperatures and for selected values of model parameters (α and γ), magnetization m and n_{HS} fraction responses are obtained as function of the variable magnetic-field, $h(t)$. In the absence of magnetic interactions ($\gamma = 0$), corresponding to Fig. 4a–c, starting from the initial conditions ($m = 0$ and $n_{HS} = 0$), the diamagnetic phases remain still stable up to $T = 35$ K (see panels a and b) but at high temperatures (panel c), paramagnetic phases prevail ($m \sim 0$ and $n_{HS} \sim 1$). Obviously, these behaviors are in agreement with different nature phases obtained in Fig. 1 where the thermal equilibrium properties of the system are studied in the previous section. For non-zero magnetic interactions cases (panels d, e and f), according to the initial value of m and n_{HS}, diamagnetic phases are the most probables delimiting a cycle as previously observed in Fig. 4a–c. It is interesting to notice that while the magnetization m oscillation frequency is exactly of that of the applied magnetic-field $h(t) = h_0 \cos(\omega_0 t)$, frequency doubling is obtained as in Ref. [54] which is attributed to the quadratic nature of $n_{HS} = \langle\sigma^2\rangle$. For $T = 40$ K, similar trends are obtained on the evolving time of m and n_{HS} behaviors (Fig. 5). In this figure, the two thermodynamic quantities, topologically fall down on limiting cycles which appear as steady phases although the initial value of m is found in overlay of stable, metastable and unstable state (Panel a) while that of n_{HS} is a metastable state (Panel b) [55]. When the initial values of the magnetization and the HS fraction are in metastable and in unstable domains (resp. $m \simeq 0$ and $n_{HS} \simeq 0.1$) as respectively, in panels c and d, first, the system's behavior is erratic and takes a lot of time to reach topological limiting cycle with a butterfly shape, characteristic of the existence of two strong attractors. These behaviors are strengthened by the existence of a dephasing between the magnetic-field h and the magnetization m (n_{HS} fraction respectively), causing the delay of the synchronization between them and which are analysed in the next sections through the frequency variations of the field energy.

To better understand system's properties along the isothermal relaxation, we analyze the temporal behavior of the both order parameters, m and n_{HS}, with selected values of model parameters throughout the four Figs. 6, 7, 8 and 9, where m (resp. n_{HS}) is represented as function of parameter ξ, for zero-magnetic field energy in green (resp. red) color and with blue (resp. black) color in the case for nonzero value of magnetic-field energy. In the absence of the magnetic-

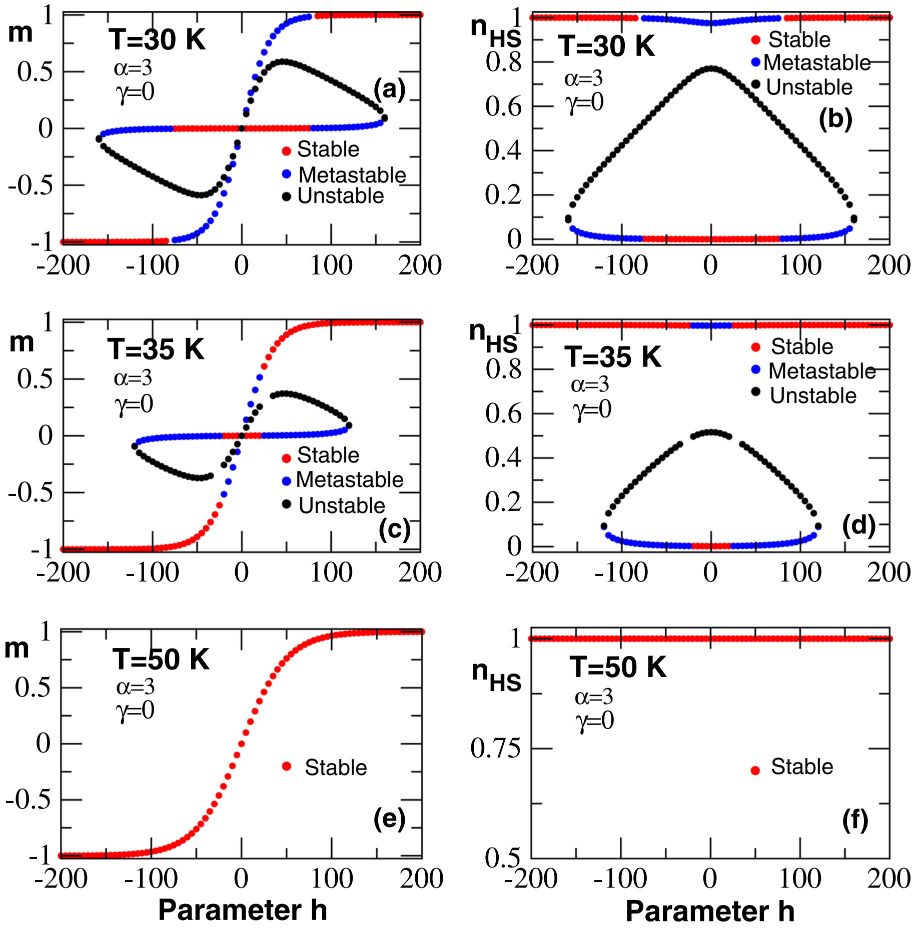

Fig. 2 Multi-spin states transition of magnetization m and n_{HS} fraction with varying magnetic-field energy for $\gamma = 0$ and $\alpha = 3$. For low temperature, intermediate spin state are got in the absence of magnetic interactions, whereas these are disappeared at high temperature as described in Ref. [55]. The color code, red, blue and black is used here to identify the stable, metastable and unstable states, respectively

field ($h = 0$), before reaching the saturation, the magnetization m (resp. HS fraction n_{HS}) relaxes towards $m = 0$ in a relatively short time (long time) which is the intrinsic timescale of the system's dynamics, which depends on the values of the intrinsic spin flip frequency $\frac{1}{\tau_0}$ and the chosen value of the intramolecular energy barrier, E_a^0, defined in Eq. 10. These limit values are smaller than the one obtained in the presence of the magnetic-field energy. Here, for more visibility these quantities (for n_{HS} values) are multiplied by a factor constant to be measurable with those of the effects of the h-field (see Figs. 6, 7 and 8) allowing the system to follow its intrinsic behavior at the time. Figures 6 and 7 are obtained in the absence of the magnetic interaction ($\gamma = 0$) with different initial conditions ($m = 0$, $n_{HS} = 0$ and $m = 0, \pm 1$, $n_{HS} = 0$ resp.) at fixed temperature of the corresponding equilibrium thermal hysteresis loop (see Fig. 1, panels a, b). In Fig. 6, all panels represent isothermal relaxations of m and n_{HS}, obtained at $T = 25, 30, 35$ and 40 K starting with the initial conditions $m = 0$ and $n_{HS} = 0$. It is found that when $\gamma = 0$, the magnetic system stays almost in the diamagnetic phase ($n_{HS} \simeq 0$) until $T = 35$ K. For higher temperatures (e.g. $T = 40$ K), the most probable state is strongly paramagnetic, with the presence of a weak ferromagnetic component, since the HS fraction, n_{HS}, reaches the maximum value 1 and the magnetization values turned around $m \sim 0.2$. To get more insights about the oscillations frequencies and the dephasing ϕ between the HS fraction, n_{HS}, the magnetization, m, and the magnetic-field, h, the temporal oscillations are calculated through $\delta n_{HS}(\xi) = n_{HS}(\xi) - < n_{HS} > (\xi)$ where the mean value of n_{HS} between two consecutive times ξ_i and ξ_{i+1} is defined as $< n_{HS} > (\xi) = \frac{1}{2}\left[n_{HS}(\xi_{i+1}) + n_{HS}(\xi_i)\right]$. Throughout all panels of this figure (Fig. 6a–d), thermodynamic quantities such as m, magnetization and n_{HS}, HS fraction are in phase and the phase shift of these in relation to the magnetic-field h is $|\phi| = \frac{2\pi}{5}$, obtained at any temperature T. The part of the instantaneous phase evolves with constant frequency as $\frac{1}{\tau_0}$ (at any temperature and for $E_0^a = 0$) which is the same for that of m and h, while that of the HS fraction, n_{HS} [54], is the double. This allows us to define a constant pulsation

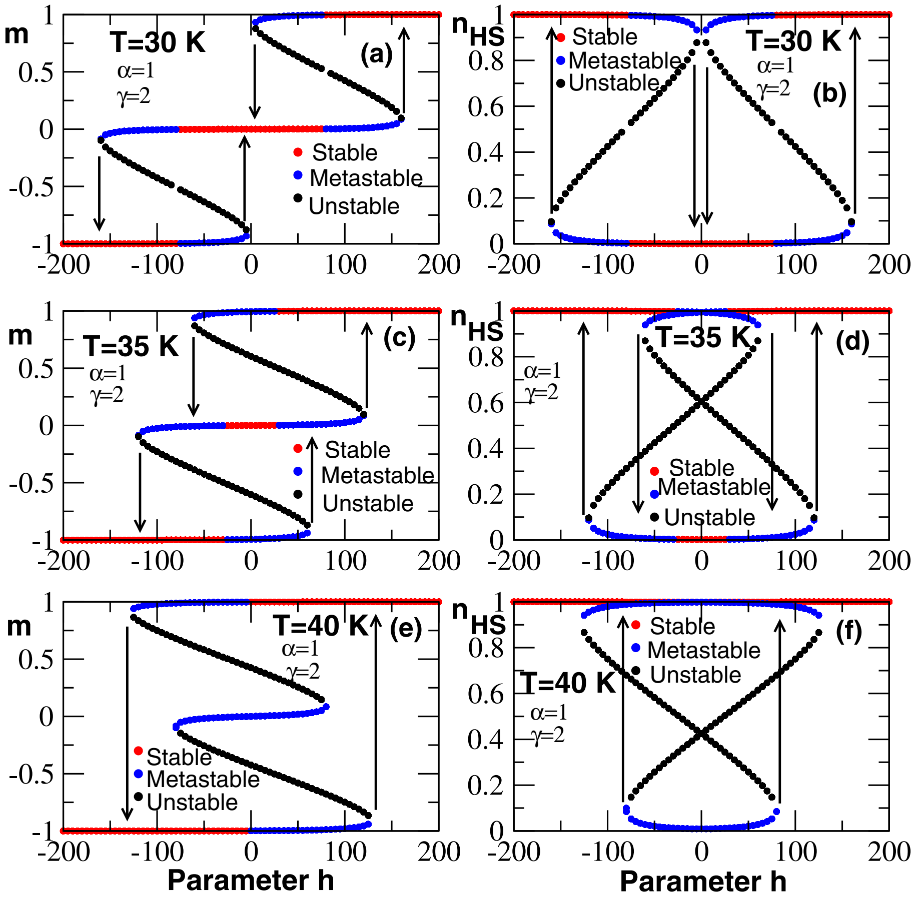

Fig. 3 Effect of the magnetic-field energy on the spin-transition in the vicinity and inside the thermal hysteresis loops of Fig. 1 for $\alpha = 1$ and $\gamma = 2$. Magnetic-hysteresis like with multistep behaviors of magnetization m and n_{HS} fraction are depicted through all panels at fixed temperature. Here, the color codes have the same meaning as in Fig. 2

$\omega_0 = 6\pi\ rad.s^{-1}$ (for m and h) such that $\omega_0\tau_0 = 2\pi$. We notice that, as far as $\lambda = 1$ the dephasing and the frequency are temperature-independent, leading to a unique dephasing value, $\phi \simeq \dfrac{2\pi}{5}$ (see Fig. 10) due to the non-linearities of the relaxation phenomenon at shot time scale. In contrast, the magnitude of the system's magnetization, m, remains always much greater than that of the HS fraction, n_{HS}, because of its quadratic character, thus enhancing the weakening of its amplitude in LS phases ($< \sigma_i^2 >= n_{HS} \ll 1$). These results are also obtained while changing either the initial conditions or the values of the different couplings between the SCO units. Not to overload the figures, these properties are folded on Fig. 8 and not on the set of these three following figures. In Fig. 7, the results are got with the initial conditions $m = 0, \pm 1$ and $n_{HS} = 0$ at fixed temperature $T = 30, 35$ and 40 K. Similar trends are obtained in the behavior of the fraction, n_{HS}, compared with those of Fig. 6, whereas, the magnetization is decreasing to $m \simeq 0$ which is the equilibrium state obtained from the initial stage. In the presence of the magnetic interactions ($\gamma \neq 0$), similar trends are obtained and presented in Figs. 8 and 9. However, according to γ values, the stable states are reached in agreement with their equilibrium values in the corresponding thermal hysteresis loop (see Fig. 1, panels c, d). In Fig. 9, from the initial conditions ($m = 0, \pm 1$, $n_{HS} = 1$), the system relaxes back to its equilibrium state [54]: the LS phases obtained at low temperature. For high temperatures regions, the saturated values of m and n_{HS} are reached where the SCO units, mostly interacted magnetically. These temperature-dependent dynamical studies allow us to substantiate the features of the spin states phases during their relaxation, where dynamical stable states accompanied with some oscillations showed by the inset in some figures have emerged, as already obtained in Ref. [54]. Thus, according to the temperature values with specific conditions, applying an oscillating magnetic-field in macroscopic bistable regions, clearly contributes to reduce the lifetime of the spin states by switching quickly the SCO system between the equilibrium phases, as depicted in panels a–f of Fig. 9. These particular results can be obtained in

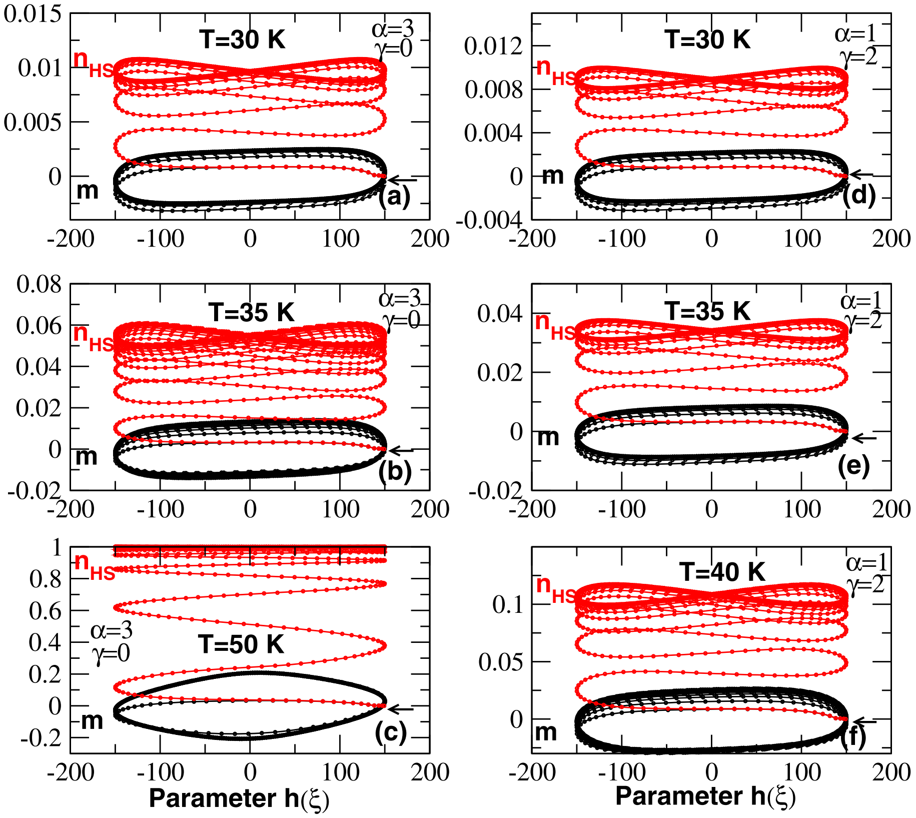

Fig. 4 Isothermal relaxation of magnetization m and n_{HS} fraction under time-dependent magnetic-field energy for selected value of model parameters $\alpha = 3$ and $\gamma = 0$ (left panels: **a**, **b** and **c**) with $\alpha = 1$ and $\gamma = 2$ (right panels: **d**, **e** and **f**). Black/red colors are used to identify m/n_{HS} curves, respectively. From initial conditions $m = 0$ and $n_{HS} = 0$ (indicated by arrows), the relaxation proceeds in time and phase synchronized with limiting cycle appears containing steady states at different temperatures near the thermal hysteresis loop of Fig. 1. In all panels, the temperature values are: $T = 30$ K (**a**) and (**d**), $T = 35$ K (**b**) and (**e**), $T = 40$ K (**f**) and $T = 50$ K (**c**)

an another way by turning the magnetic field frequencies as discussed in the next section.

3.3 Effects of magnetic-field frequencies on isothermal relaxation curves with $J = 0$

Now, we investigate the effect of the magnetic-field frequency on the behaviour of the order parameters m and n_{HS} for different values of control parameter, λ, which regulates the value of the oscillation frequency of the applied field h. In Fig. S1, for $\alpha = 3$ and $\gamma = 0$, isothermal relaxation of the system is depicted for $T = 30$ K. From the initial values of m and n_{HS}, on gets limiting cycles whose areas increase with the field energy frequencies. Then, the both parameter m and n_{HS} superimposed with the magnetic-field for low frequencies (with long periods). When the initial values of n_{HS} fraction and the magnetization m are zero, the magnetic-field in one period shifts the spin states such that $0 \leq n_{HS} \leq 0.031$ and $-0.031 \leq m \leq +0.031$ respectively, (Fig. S1a and S1g), which are decreasing in magnitude when, λ, the control parameter increases that are observed through all panels. With $m = 0$, intermediate spin states can appear when the magnetization m frequency is that of the magnetic-field while the n_{HS} frequency's is doubling (see panels a–l). With nonzero initial conditions (e.g. $m = 0.25$ and $n_{HS} = 0.98$ for panels c and i of Fig. S1) and for low $\lambda(= 0.05)$ values, it is possible to shift the spin states under the dynamical action of the magnetic-field, $h(t)$, such that $-1 \leq m \leq +1$ and $n_{HS} \simeq 1$. In this situation, the magnetic-field clearly switches the SCO system between the two ferromagnetic states characterized by the magnetizations $m = +1$ and $m = -1$, while the system keeps the HS state. From this point of view, the system get its equilibrium values and fall down on limiting cycle as hysteretic-like where different states are switching up to their saturated values. Obviously, following a long period, the n_{HS} fraction frequency is the double of that of the magnetic-field energy (as well as of the magnetization m) as described in the previous section. In Fig. S2, the system behavior is analyzed at $T = 40\ K$ with different initial conditions ($m = +1$, $n_{HS} = 1$ for panels a–d and panels g–j resp. and $m = 0$, $n_{HS} = 1$ for panels e–f and for panels k–l resp.). Similar trends are observed where the system is stabilized on limiting cycles likely a magnetic hysteresis loop on m curves for low $\lambda(\leq 1)$ values as previously observed in Fig. S1 when $-1 \leq m \leq +1$ and $n_{HS} \simeq 1$ (see panels a–f and g–l resp.). It is worth to mention that the symmetric

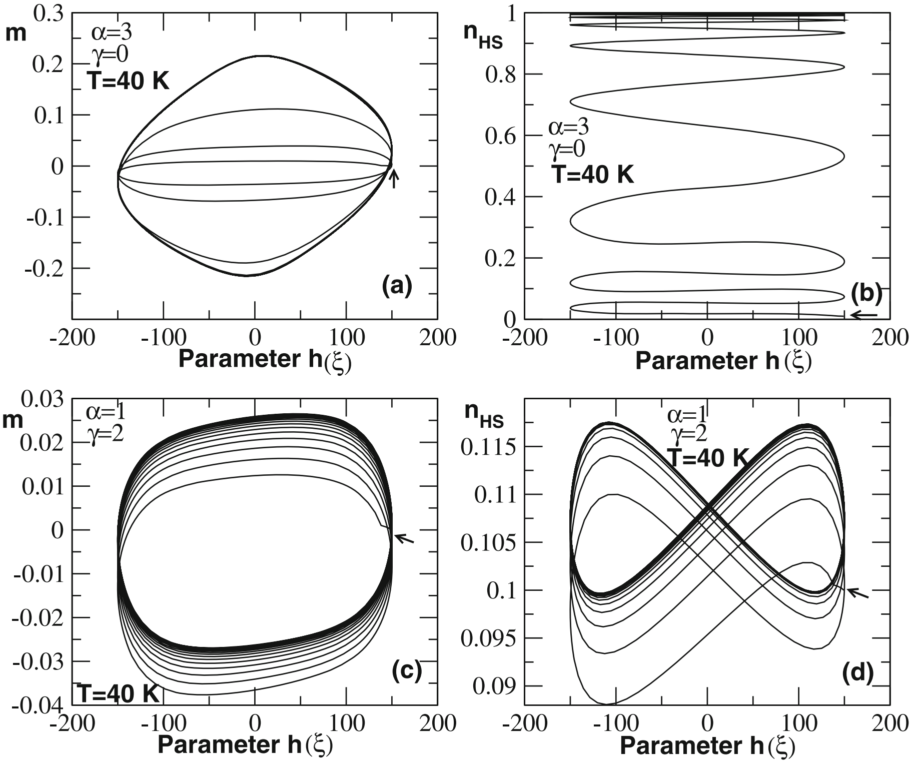

Fig. 5 Isothermal relaxation of magnetization m and n_{HS} fraction under time-dependent magnetic-field energy for selected value of model parameters $\alpha = 3$ and $\gamma = 0$ (top panels: **a** and **b**) and $\alpha = 1$ and $\gamma = 2$ (bottom panels: **c** and **d**). From initial conditions (rep. $m = 0$; $n_{HS} = 0$ and $m = 0$; $n_{HS} = 0.1$ in panels **a**, **b** and in panels **c**, **d** indicated by arrows), the relaxation proceeds in time and phase synchronized with limiting cycle appears containing steady states at $T = 40$ K inside the thermal hysteresis loop of Fig. 1. In panel **d**, n_{HS} fraction appears with erratic behaviors and then fall down on limiting cycle which appears as metastable states (see text)

(resp. anti-symmetric) character of n_{HS} (resp. m) with respect to $h(\lambda\xi)$ is kept in some panels of Figs. S1, S2, S3, S4, S5 and S6. When the temperature increases, the stable states are obtained for $n_{HS} \simeq 1$ where thermal spin states have been created (Fig. 1). Applying the magnetic-field energy at this stage, help to obtain novel properties of the system although the magnetization is zero ($m = 0$) from which steady states appear along the magnetic hysteresis loop for low frequencies of the field energy (see Figs. S1, S2 and S3). One can conclude that, without the exchange magnetic interactions, it is possible to create intermediate spin states through the magnetic-field energy for varying their frequencies.

3.4 Magnetic-field frequencies effects on isothermal relaxation curves in the presence of magnetic exchange interactions ($J \neq 0$)

Here, we analyze the system behaviors in the presence of both elastic and magnetic interactions accounting for spin-phonon interactions. Then, spin states are created and magnetic interactions take place in HS phases. The system configurations are relaxed in time along the magnetic-field energy with different frequencies values controlled by the parameter λ as shown in Fig. S4. Throughout all panels for this figure, the results bear some resemblances for that obtained in Fig. S1 excepted for panels (c) and (i) for each figure (see Figs. S1 and S4) where the initial values are quite different ($m = 0.25$; $n_{HS} = 0.98$ and $m = 0.025$; $n_{HS} = 0.03$), respectively. This can explain by the fact that at low temperature ($T = 30$ K), in the presence ($\gamma \neq 0$) or the absence ($\gamma = 0$) of magnetic interactions, the most common states probably stable are for $m = 0$ and $n_{HS} = 0$ corresponding to the LS states (diamagnetic phase) where γ have not significant effects on the spin move processes. However, increasing the frequencies values enlarge the domain of limiting cycle always obtained around $m \sim 0$ and $n_{HS} \sim 0$. Then, the magnitude of the average spin values ($\langle\sigma\rangle$ and $\langle\sigma^2\rangle$) decreases with the frequencies values (e.g. $-0.034 \leq m \leq +0.034$ and $0 \leq n_{HS} \leq 0.034$ in panels a and g resp.; $-0.025 \leq m \leq +0.025$ and $0 \leq n_{HS} \leq 0.025$ in panels b and h resp.) for $\lambda = 0.01$ and $\lambda = 0.05$, respectively. Furthermore, when the initial values of $n_{HS} \simeq 1$ with significant value of m, the magnetic field lift the system degeneracy for crossing magnetic hysteresis cycle likely (Panels c and i). Figure S5 is obtained at $T = 35$ K and for the same model parameters as in Fig. S4. It is straight forwarded to notice that the initial values of the magnetization (m) and of the HS fraction (n_{HS}) are that of the system subject to nonmagnetic field energy where the spin states are thermally induced (Fig. 1). Once the system is in contact with the magnetic source

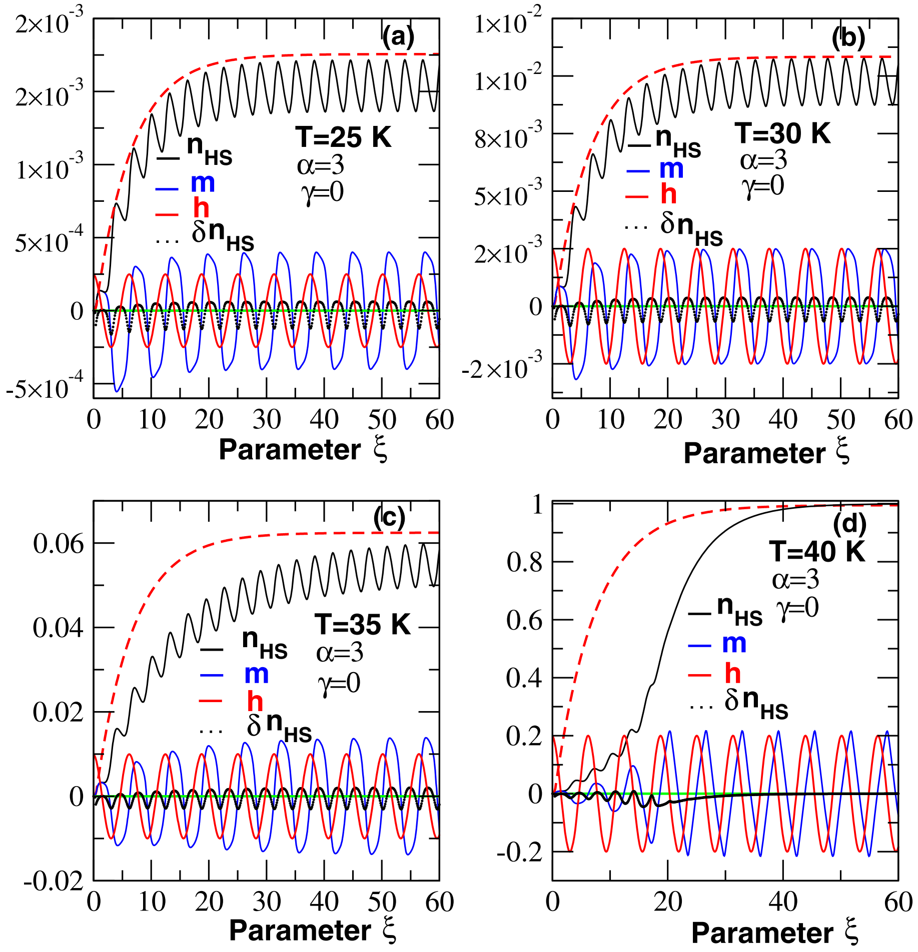

Fig. 6 Time-dependent behavior of magnetization m and n_{HS} fraction in responses by applying magnetic-field energy with selected values of model parameters $\alpha = 3$ and $\gamma = 0$. These results are obtained at fixed temperature: **a** $T = 25$ K, **b** $T = 30$ K, **c** $T = 35$ K and **d** $T = 40$ K. The red/green colors indicated the behavior of n_{HS} (dashed curve)/m (straight curve), respectively, in the case of zero-magnetic field energy. Whereas, black and blue colors indicate the behavior of n_{HS} and m, respectively, in the presence of magnetic-field energy (red curve). Comparative results are obtained with the magnetic-field energy and the n_{HS} oscillations δn_{HS} (in black dots). Diamagnetic phases are obtained with some oscillations at low temperatures whereas at high temperature, paramagnetic phases prevail with saturation value of n_{HS} fraction in the equilibrium states

energy, the magnetic spin states are created according to its frequency. One can observe that in panels (a) and (g) of Fig. S5, from $m = 0$ and $n_{HS} = 0$, the system can visit new states created by the magnetic-field where the magnetization and the HS fraction varying as $-1 \leq m \leq +1$ and $0 \leq n_{HS} \leq 1$, respectively for $\lambda = 0.01$. In panels (b) and (h), λ is set to 0.05 and from the stable states $m = 0$ and $n_{HS} = 0$, the system evolves up to $m = -1$ and $n_{HS} = 1$ which are metastable states and thermally created in Fig. 1. As the magnetic-field decreased from 150 to -150 K, the system would have chosen to decrease its magnetization from 0 to -1 then increases it again to 0 by increasing the field, while the HS fraction varying between 0 and 1. The magnetic-field energy oriented the system toward states of "spin down" ($-1 \leq m \leq 0$ and $0 \leq n_{HS} \leq 1$) for that spin transition occurs between 0 and -1 (Panels b and h). But the opposite phenomenon occurs when the relaxation starts from $n_{HS} = 0.5$ with $m = 0$ (panels c and i) and then asymmetric relaxation curves are obtained, compared with those of Fig. S5b and S5h for $\lambda = 0.05$. Indeed, for superimposing the both panels, respectively obtained on m and n_{HS} curves, symmetric properties appeared which are already debated in Ref. [55]. Thus, the magnetization clearly fulfills the relation $m(-h) = -m(h)$, it is then anti-symmetric while the HS fraction is clearly symmetric with respect of the inversion of the field, $n_{HS}(-h) = n_{HS}(h)$. Moreover, for $T = 40$ K in Fig. 1, the most stable states are described by $m = \pm 1$ and $n_{HS} = 1$ (paramagnetic phase in HS states) where the free energy is the lower as possible [55]. In Fig. S6, for low frequencies (e.g. $\lambda = 0.01$, panels a and g), new spin states are created according to the magnetic-field strength where limiting cycle appear with $-1 \leq m \leq 1$ and $0 \leq n_{HS} \leq 1$ domains although the initial values are $m = 0$ and

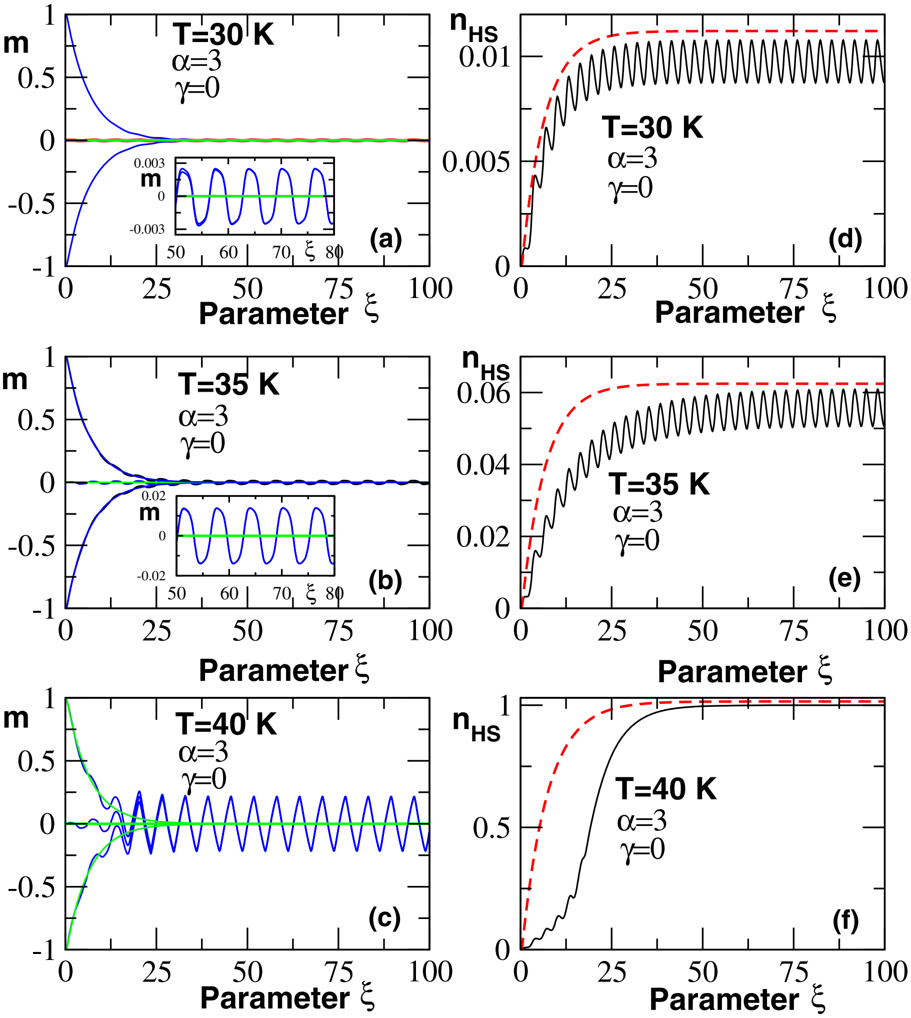

Fig. 7 Time-dependent behavior of magnetization m (panels **a**–**c**) and n_{HS} fraction (panels **d**–**f**) in responses by applying magnetic-field energy with selected values of model parameters $\alpha = 3$ and $\gamma = 0$. These results are also obtained at fixed temperature: **a** and **d** $T = 30$ K, **b** and **e** $T = 35$ K, **c** and **f** $T = 40$ K. The different color codes used here have the same meaning as in Fig. 6 by identifying m and n_{HS} behaviors. Here, the initial conditions are $n_{HS} = 0$ and $m = 0, \pm 1$ whereas in Fig. 6, $n_{HS} = 0$ and $m = 0$. In the equilibrium states, LS phases are got with some oscillations (shown by the inset figures) as obtained in Fig. 6 at low temperatures, whereas, in paramagnetic phase, n_{HS} reaches its saturated value at high temperature

$n_{HS} = 0$. When the magnetic frequency increases, the spin state decreases in magnitude as already obtained in previous figures (see panels a-l of Figs. S4, S5 and S6). In the metastable domain ($m = 0$ and $n_{HS} = 0$), the magnetic-field can only turn the spins values around zero (e.g. panels e and k for $\lambda = 0.5$). From this, it is possible with the magnetic-field energy to reveal new spin states which are turned around its initial values either $m = 0, \pm 1$ and $n_{HS} = 0, 1$.

In addition, the phase shift between m and h is represented in Fig. 10 as a function of the frequency (through $0 \leq \lambda \leq 1$) of the h-field in LS phases at different temperatures values, selected along the thermal hysteresis loop in zero-field case (Fig. 1). It is revealed that, whatever the absence (panel a) or the presence (panel b) of the magnetic interaction, this phase shift, denoted here, ϕ, is an increasing function of λ, which saturates beyond $\lambda \simeq 0.6$, where ϕ tends asymptotically to the value, $\dfrac{2\pi}{5}$. As the temperature increases, the phase shift only slightly decreases, and one may consider this quantity as being temperature-independent. On the other hand, the frequency of the HS fraction, n_{HS} is the double of that of the magnetization m, while it stays in phase with the magnetization such that by following the frequency, $\dfrac{\lambda}{\tau_0}$. As expected, the temporal dephasing δt (in insert Figure) deduced here, prints a delay in response to the action of the field energy h, and this quantity gradually decreases and converges to the same point whatever the temperature, in line with the behavior of ϕ as function of λ.

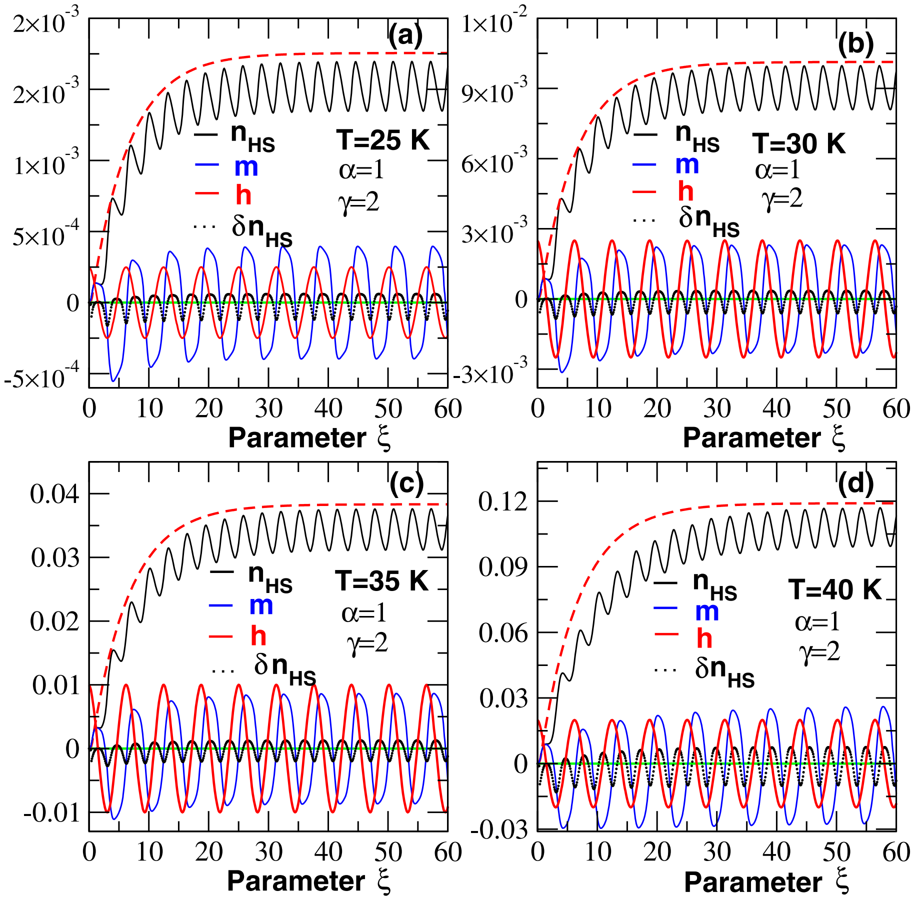

Fig. 8 Time-dependent behavior of magnetization m and n_{HS} fraction in responses by applying magnetic-field energy with selected values of model parameters $\alpha = 1$ and $\gamma = 2$. These results are obtained at fixed temperature: **a** $T = 25$ K, **b** $T = 30$ K, **c** $T = 35$ K and **d** $T = 40$ K. The different color codes and patterns used here are the same meaning as in Fig. 6 by identifying m, n_{HS}, h and δn_{HS} behaviors. Similar trends are obtained as in Fig. 6 with same initial conditions ($n_{HS} = 0$ and $m = 0$) which are here, almost metastable

To partially summarize, we recall that, the system studied here is more sensitive to an applied radio-frequency magnetic-field, which makes the investigated SCO phenomenon time-dependent, where several timescales may compete. Indeed, in addition to the timescale imposed by the excitation (the magnetic-field), the SCO system has its intrinsic timescale for the evolution of the order parameters (m and n_{HS}) which relax in the free energy landscape, leading to non-linear effects. Depending on the oscillation period of the magnetic-field with respect to the intrinsic relaxation times of the order parameters, which also depend on the initial states ($m(t = 0)$ and $n_{HS}(t = 0)$), the SCO system may be insensitive to the magnetic-field (high frequency case) or may couple dynamically to the field, generating limit cycles or highly non-linear behaviours, mostly observed on the HS fraction parameters, through butterfly pictures, recalling Lorentz attractors observed in chaos. In this case, the magnetization and the HS fraction responses to the magnetic-field excitation doe not follow in the adiabatic way the temporal behavior of $h(t)$. Throughout physical thermodynamic quantities, it is possible to amplify the magnetic order signal according to the low frequencies, either in absence or in the presence of the magnetic interaction between the different units of the SCO molecules. This is due to a technological interest in the low frequencies introduced, which are therefore better favoured by ensuring a certain stability of the different states towards rapid synchronization according to the system response.

4 Conclusion

Isothermal relaxation of BEG-like Hamiltonian under a radio-frequency time-dependent magnetic field describing SCO materials and PBAs is investigated by turning model parameters, like the frequency and the amplitude of the applied magnetic-field, as well as the strength of the elastic interactions between the SCO units. In this study, we Considered that the nn atoms are coupled via magnetic and elastic interactions propagated throughout the lattice configuration which are temperature-

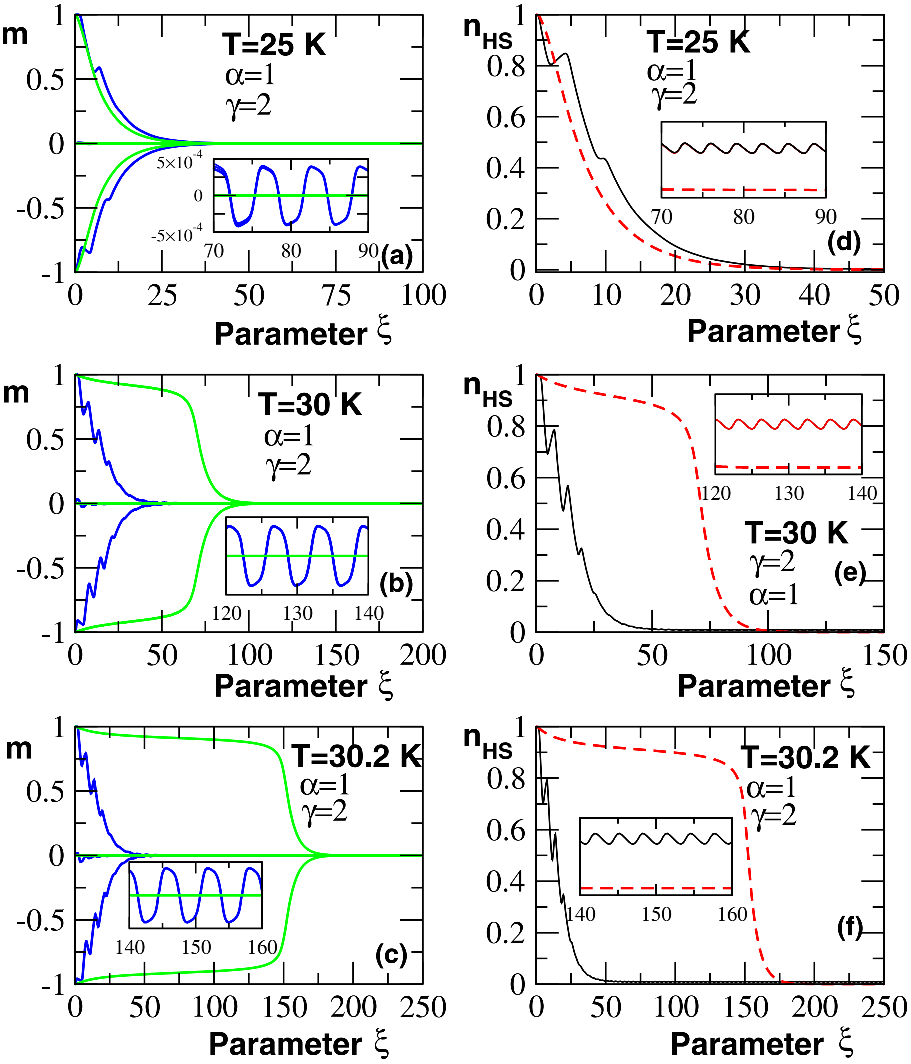

Fig. 9 Time-dependent behavior of magnetization m (panels **a**–**c**) and n_{HS} fraction (panels **d**–**f**) in responses by applying magnetic-field energy with selected values of model parameters $\alpha = 1$ and $\gamma = 2$. These results are also obtained at fixed temperature: **a** and **d** $T = 25$ K, **b** and **e** $T = 30$ K, **c** and **f** $T = 30.2$ K. The different color codes and patterns used here are the same meaning as in Fig. 6 by identifying m, n_{HS} behaviors. The relaxation started from initial conditions $n_{HS} = 1$ and $m = 0, \pm 1$ for reaching the steady states (resp. $n_{HS} \sim 0$ and $m \sim 0$) obtained as diamagnetic phases. When the temperature increases, m and n_{HS} values remain still at 1 with long relaxation time as far as the freely system evolves whereas, the h-field energy reduces the relaxation time at high temperatures

dependent to account for spin-phonon interactions. The system is also subject to radio-frequency magnetic-field with a variable oscillation frequency pushing the system to a dynamical equilibrium following limiting cycles in the space $m - h$ and $n_{HS} - h$ with clear evidence of dephasing between the responses diagrams of the two order parameters, as a result of the system's non-linearity's. The magnitude of the key thermodynamic parameters (m and n_{HS} fraction) are decreasing function as the frequency increases. As demonstrated in previous works, LS and HS states are thermally induced and become fundamental states in equilibrium cases. From the initial conditions, the evolving equation obtained in the framework of the dynamic mean-field theory (DMFT) revealed the different states (phases) through the magnetic-field frequencies and becomes as the key parameter for reconstitution of information storage or displays, memories, related to the multi-stability system as much debated in Ref. [55]. These spin-transition phenomena are temperature-dependent and intrinsically related to the magnetic-field frequency which is exactly the one of the magnetization $m = \langle\sigma\rangle$ and exhibited the frequency doubling of the HS fraction, $n_{HS} = \langle\sigma^2\rangle$, where σ is the spin state. Extensions of this work will consider true elastic interactions between the spin states, instead of the phenomenological elastic term K with both magnetic exchange interaction J and magnetic-field $h(t)$, in

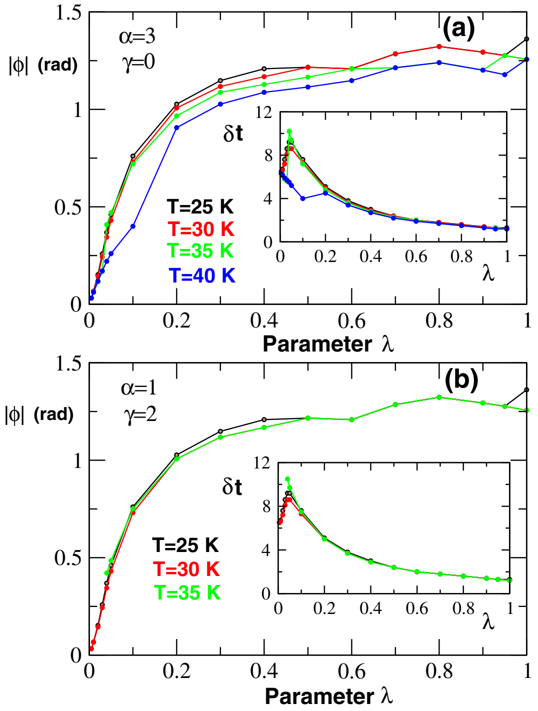

Fig. 10 Phase shift between the magnetization m and the time-dependent magnetic-field energy as function of the reduced parameter λ of the magnetic-field frequency for selected values of temperature in the corresponding thermal hysteresis loop of Fig. 1. In the absence (panel **a**) or in the presence (panel **b**) of the magnetic interaction, the dephasing $|\phi|$ is an increasing function of λ at each temperature. The insert figure is related to the temporal shift δt which is a decreasing function with the parameter λ. All the curves tend to the same value as far as $\lambda \sim 1$ where $|\phi| \simeq \frac{2\pi}{5}$ (see text). The other model parameters are written in the Figure

the scheme of an adapted dynamical mean field theory (MFT).

Acknowledgements This research was funded by ANR (Agence Nationale de la Recherche Scientifique), grant number Mol-CoSM N° ANR-20-CE07-0028-02 and the Universities of Versailles and Paris-Saclay-UPSAY, the CNRS (Centre National de la Recherche Scientifique) and LIA (International Associate French Japan Laboratory). T.D. OKE acknowledges financial support from the “Groupe d’Etudes de la Matière Condensée” (GEMaC) of the “Université de Versailles Saint-Quentin” during a visit.

Author contributions

All authors equally contribute to the present work in the calculations and in the manuscript writing process.

Data Availability Statement This manuscript has associated data in a data repository. [Authors’ comment: Numerical results are obtained with ForTran Code based on evolving system equations and help us to display all Figures reported in this paper, which are available on request by T. D. OKE.]

Declarations

Conflict of interest All authors approve for submission and declare that they have no known competing financial interests as well as no conflict of personal relationships that could have influenced the obtained results. The authors declare that this original manuscript is not currently being considered for publication elsewhere.

References

1. P. Gütlich, H.A. Goodwin, *Spin-Crossover in transition Metal Compounds I, II and III* (Springer, Berlin, 2004), pp. 233–235
2. J.H. Ammeter, Nov. J. Chem. **4**, 631 (1980)
3. S. Ohkoshi, K. Hashimoto, J. Am. Chem. Soc. **121**, 10591 (1999)
4. S. Ohkoshi, S. Ikeda, T. Hozumi, T. Kashiwagi, K. Hashimoto, J. Am. Chem. Soc. **128**, 5320 (2006)
5. S. Ohkoshi, K. Imoto, Y. Tsunobuchi, S. Takano, H. Tokoro, Nat. Chem. **3**, 564 (2011). https://doi.org/10.1038/nchem.1067
6. P. Gütlich, A. Hauser, H. Spiering, Angew. Chem. Int. Ed. **33**, 2024 (1994)
7. J.M. Herrera, V. Marvand, M. Verdager, J. Marrot, M. kalisz, C. Mathoniere, Angew. Chem. Int. Ed. **43**, 5468 (2004)
8. N. Nègre, C. Conséjo, M. Goiran, A. Bousseksou, F. Varret, J.P. Tuchagues, R. Barbaste, S. Askénazy, J.G. Haasnoot, Phys. B **294–295**, 91 (2001)
9. H. Tokoro, S.-I. Ohkoshi, K. Hashimoto, Appl. Phys. Lett. **82**, 1245 (2003)
10. F. Varret, K. Boukheddaden, C. Chong, A. Goujon, B. Gillon, J. Jeftic, A. Hausser, Eur. Phys. Lett. **77**, 30007 (2007)
11. D.A. Pejakovíc, J.L. Maison, C. Kitamura, J.S. Miller, A.J. Epstein, Polyhedron **20**, 1435 (2001)
12. K. Kato, Y. Moritomo, M. Takata, M. Sakata, M. Umekawa, N. Hamada, S. Ohkoshi, H. Tokoro, K. Hashimoto, Phys. Lett. **91**, 255502 (2003)
13. H. Banerjee, S. Chakraborty, T. Saha-Dasgupta, Inorganics **5**, 47 (2017)
14. A. Gîndulescu, A. Rotaru, J. Linares, M. Dimian, J. Naser, J. Phys: Conf. Ser. **268**, 012007 (2011)
15. M. Nishino, S. Miyashita, P.A. Rikvold, Phys. Rev. B **96**, 144425 (2017)
16. C. Enashescu, L. Stoleriu, A. Stancu, A. Hausser, Phys. Rev. B **82**, 104114 (2010)
17. M. Sorai, S. Seki, J. Phys. Chem. Solids **35**, 555 (1974)
18. M.M. Dîrtu, C. Neuhausen, A.D. Naik, A. Rotaru, L. Spinu, Y. Garcia, Inorg. Chem. **49**, 5723 (2010)
19. W. Nicolazzi, J. Pavlik, S. Bedoui, G. Molnár, A. Bousseksou, Eur. Phys. J. Spec. Topics **222**, 1137 (2013)
20. M. Paez-Espejo, M. Sy, K. Boukheddaden, J. Am. Chem. Soc. **138**, 3202 (2016)
21. M.A. Halcrow, *Spin-Crossover Materials: Properties and Applications* (Wiley, New York, 2013)

22. P. Gütlich, A.B. Gasper, Y. Garcia, Beilstein J. Org. Chem. **9**, 342 (2013)
23. C.M. Quintero, G. Félix, I. Suleimanov, J.S. Costa, G. Molnár, L. Salmon, W. Nicolazzi, A. Bousseksou, Beilstein J. Nanotechnol. **5**, 2230 (2014)
24. E. König, Struct. Bond. **7**, 51 (1991)
25. H. Spiering, N. Willenbacher, J. Phys.: Condens. Matter **1**, 10089 (1989)
26. Y. Ogawa, A. Mino, S. Keshihara, K. Koshino, T. Ogawa, C. Urano, H. Tagaki, Phys. Rev. Lett. **84**, 3181 (2000)
27. K. Boukheddaden, J. Linares, H. Spiering, F. Varret, Eur. Phys. J. B **15**, 317 (2000)
28. K. Boukheddaden, I. Shteto, B. Hôo, F. Varret, Phys. Rev. B **62**, 14796 (2000)
29. K. Boukheddaden, I. Shteto, B. Hôo, F. Varret, Phys. Rev. B **62**, 14806 (2000)
30. M. Nishino, S. Miyashita, Phys. Rev. B **63**, 174404 (2001)
31. M. Nishino, K. Boukheddaden, S. Miyashita, F. Varret, Phys. Rev. B **72**, 064452 (2005)
32. K. Boukheddaden, M. Nishino, S. Miyashita, F. Varret, Phys. Rev. **72**, 014467 (2005)
33. H. Watanabe, N. Bréfuel, S. Mouri, J.-P. Tuchagues, E. Collet, and Tanaka. Eur. Phys. Lett. **96**, 17004 (2011)
34. K. Boukheddaden, M. Sy, F. Varret, M. Paez-Espejo, A. Slimani, F. Varret, Phys. Rev. B **486**, 187 (2016)
35. M. Paez-Espejo, M. Sy, F. Varret, K. Boukheddaden, Phys. Rev. B **89**, 024306 (2014)
36. C. Chong, F. Varret, K. Boukheddaden, Phys. Rev. B **81**, 014104 (2010)
37. C. Enachescu, R. Tanasa, A. Stancu, F. Varret, J. Linares, E. Codjovi, Phys. Rev. B **72**, 054413 (2005)
38. M. Sy, D. Garrot, A. Slimani, M. Paez-Espejo, F. Varret, K. Boukheddaden, Angew. Chem. **55**, 1755 (2016)
39. K. Boukheddaden, Eur. J. Inorg. Chem. https://doi.org/10.1002/ejic.201201093
40. B. Hôo, K. Boukheddaden, F. Varret, Eur. Phys. J. B **17**, 449 (2000)
41. A. Slimani, F. Varret, K. Boukheddaden, D. Garrot, H. Oubouchou, S. Kaizaki, Phys. Rev. Lett. **110**, 087208 (2013)
42. H. Romstedt, A. Hauser, H. Spiering, J. Phys. Chem. Solids **59**, 265 (1998)
43. K. Boukheddaden, F. Varret, S. Salinke, J. Linares, E. Codjovi, Phase Trans. **75**, 733 (2002)
44. S. Mouri, K. Tanaka, S. Bonhommeau, N.O. Moussa, G. Molnár, A. Bousseksou, Phys. Rev. B **78**, 174308 (2008)
45. A. Bousseksou, J. Nasser, J. Linares, K. Boukheddaden, F. Varret, J. Phys. I **2**, 1381 (1992)
46. A. Bousseksou, F. Varret, J. Nasser, J. Phys. I **3**, 1463 (1993)
47. N. Sasaki, T. Kambara, J. Phys. C **15**, 1035 (1982)
48. A. Bousseksou, N. Nègre, M. Goiran, L. Salmon, J.-P. Tuchagues, M.-L. Boillot, K. Boukheddaden, F. Varret, Eur. Phys. J. B **13**, 451 (2000)
49. A. Bousseksou, F. Varret, M. Goiran, K. Boukheddaden, J.-P. Tuchagues, Top. Curr. Chem. **235**, 65 (2004)
50. A. Bousseksou, K. Boukheddaden, M. Goiran, C. Consejo, M.-L. Boillot, J.-P. Tuchagues, Phys. Rev. **65**, 172412 (2002)
51. S. Bonhommeau, G. Molnár, M. Goiran, K. Boukheddaden, A. Bousseksou, Phys. Rev. B **74**, 064424 (2006)
52. J.L. Her, Y.H. Matsuda, M. Nakano, Y. Niva, Y. Inada, J. Appl. Phys. **111**, 053921 (2012)
53. Y. Garcia, O. Kahn, J.-P. Ader, A. Buzdin, Y. Meurdesoif, M. Guillot, Phys. Lett. A **271**, 145 (2000)
54. S.B. Ogou, T.D. Oke, F. Hontinfinde, K. Boukheddaden, Adv. Theory Simul. **2**, 1800192 (2019)
55. T.D. Oke, M. Ndiaye, F. Hontinfinde, K. Boukheddaden, Eur. Phys. J. B **94**, 38 (2021)
56. T.D. Oke, F. Hontinfinde, K. Boukheddaden, Eur. Phys. J. B **86**, 271 (2013)
57. T.D. Oke, F. Hontinfinde, K. Boukheddaden, Appl. Phys. A **120**, 309 (2015)
58. T.D. Oke, F. Hontinfinde, K. Boukheddaden, Comput. Condens. Matter **9**, 27 (2016)
59. M. Nishino, K. Boukheddaden, S. Miyashita, F. Varret, Polyhedron **24**, 2852 (2005)
60. M. Nishino, K. Boukheddaden, S. Miyashita, F. Varret, Phys. Rev. B, **68**, 224402 (2003) (references therein)
61. G. D'Avino, A. Painelli, K. Boukheddaden, Phys. Rev. B **84**, 104119 (2011)
62. T. Sauer, *Numerical Analysis*, 2nd edn. (Pearson Education, Inc., Hoboken, 2012)
63. R.L. Burden, J.D. Faires, *Numerical Analysis*, 9th edn. (Cengage, Boston, 2010)
64. A. Quarteroni, R. Sacco, F. Saleri, *Méthodes Numériques: Algorithmes, analyse et applications* (Springer-Verlag, Milano, 2007)
65. S.D. Conte, C. de Boor, *Elementary Numerical Analysis: An Algorithmic Approach*, 3rd edn. (McGraw-Hill, New-York, 1980)